

Control of photoelectron interference in asymmetric momentum distributions using two-color laser fields

Xu Zheng,¹ Ming-Ming Liu,¹ Hui Xie,² Peipei Ge,¹ Min Li,^{1,2,*} and Yunquan Liu^{1,3}

¹*Department of Physics and State Key Laboratory for Mesoscopic Physics, Peking University, Beijing 100871, People's Republic of China*

²*School of Physics and Wuhan National Laboratory for Optoelectronics, Huazhong University of Science and Technology, Wuhan 430074, People's Republic of China*

³*Collaborative Innovation Center of Quantum Matter, Beijing 100871, People's Republic of China*

(Received 24 August 2015; revised manuscript received 12 October 2015; published 23 November 2015)

We theoretically study the control of photoelectron interference of atoms ionized by a two-color laser field with parallel polarizations. Based on both the quantum-trajectory Monte Carlo model and an *ab initio* simulation with numerically solving the time-dependent Schrödinger equation, we show that the photoelectron angular distributions can be controlled by changing the relative phase of the two frequency components. The high-energy and low-energy photoelectrons show different modulations with respect to the relative phase. Tracing back to the initial coordinates (the ionization time with respect to the laser phase and the initial momentum) of photoelectrons, we have studied the physical origin of the asymmetric structure in photoelectron angular distributions and the dynamics of controlling photoelectron emission using the two-color laser fields. We show that the long tail of the Coulomb potential plays a minor role in the position of the high-energy cutoff in the backward scattering, whereas it is of great importance in the formation of the asymmetric structures of the low-energy photoelectrons.

DOI: [10.1103/PhysRevA.92.053422](https://doi.org/10.1103/PhysRevA.92.053422)

PACS number(s): 32.80.Qk, 32.80.Fb, 32.80.Rm

I. INTRODUCTION

Tunneling ionization and multiphoton ionization are two main processes when an atom is exposed to a strong laser field. The ionization processes will be dominated by multiphoton ionization when $\gamma \gg 1$ and by tunneling ionization when $\gamma \ll 1$, where $\gamma = \sqrt{I_p}/2U_p$ is the Keldysh parameter, I_p is the ionization potential, and $U_p = E_0^2/4\omega^2$ is the ponderomotive energy [1]. After detachment from atoms, the released electron wave packets following different pathways to the same final state will give rise to quantum interference. Photoelectron interference from strong-field ionization encodes a wealth of information about the dynamics of the nucleus and photoelectrons [2,3], which can be used to resolve the ionization dynamics and to extract the structural information of molecules.

The general features of photoelectron energy spectra can be qualitatively understood in terms of the semiclassical picture [4]. In a linearly polarized laser field, the energy of photoelectrons, which are directly accelerated away from the nucleus after tunneling, can extend up to $2U_p$, which is the onset of the well-known plateau region in photoelectron energy spectra. If the photoelectron is driven back by the oscillating laser field and is backscattered upon its parent ion, its kinetic energy can be promoted up to $10U_p$, which is the well-known high-energy cutoff observed in photoelectron energy spectra [4–6]. Besides those general features, the interference effect also plays an important role in the photoelectron energy spectra. The intercycle interference of electron wave packets gives rise to the above-threshold ionization (ATI) peaks [7] which are separated by one-photon energy ω in the photoelectron energy spectra [8]. The intracycle interference induced by the recollision can be used to measure the photoelectron holograms of atoms and molecules [2,3,9–11].

Precise manipulation of the electron dynamics is the primary step towards developing interferometric technology to probe ultrafast multielectron dynamics [12] and to control chemical reactions. There are many experimental “knobs” that can be used to achieve this manipulation, such as the pump-probe delay and the carrier envelope phase of a few-cycle laser pulse [13–15]. Recently, the control of ionization processes and electron dynamics using multicolor fields has attracted both experimental and theoretical interests [16,17]. Two-color laser fields with parallel polarizations have many important applications, e.g., probing quantum phase shifts and electron delays in ATIs [18,19], generating terahertz waves and high harmonics [20,21], and retrieving the structures and dynamics of valence-electron clouds in atoms [22,23]. Recently, Skruszewicz *et al.* have investigated the change in electron yield as a function of the relative phase of parallel two-color fields by introducing relative-phase-contrast and phase-of-the-phase spectra [24]. Using orthogonally polarized two-color laser fields, one can control the interference of photoelectron wave packets in both temporal and spatial domains [25,26] and the electron-electron correlation in double ionization [27].

In the present paper, we study the control of electron dynamics of atoms in two-color laser pulses consisting of 800-nm (strong) and 400-nm (weak) fields with parallel polarizations. We use two different approaches to calculate the photoelectron angular distributions (PADs), i.e., the quantum-trajectory Monte Carlo (QTMC) model and numerical solution of the time-dependent Schrödinger equation (TDSE). We show that the relative phase of the two-color components can act as a knob to control the electron emissions as well as the interference patterns with attosecond precision. Taking advantage of the QTMC model [28,29], we investigate the physical origin of different interference patterns and study the influence of the Coulomb potential on the photoelectron momentum spectra. We find that the long tail of the Coulomb potential has a minor effect on the position of photoelectron

*minli@pku.edu.cn

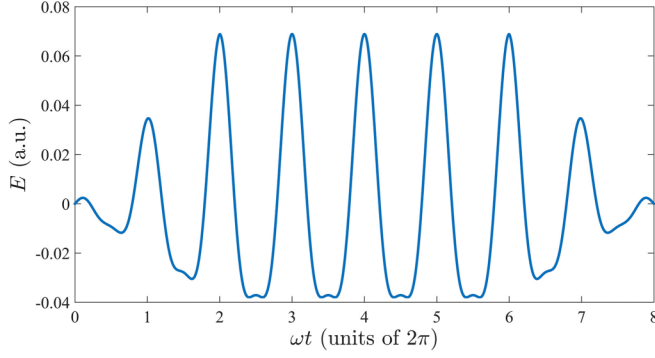


FIG. 1. (Color online) The typical two-color laser field of Eq. (1) for $\varphi = 0$. An eight-cycle trapezoidal pulse is used in our calculation with a two-cycle turn on and turn off for 800 nm.

energy cutoff in the backward scattering for the two-color field. Tracing the low-energy electrons back to the initial coordinates at the tunnel exit, we shed light on the importance of the long-range Coulomb potential in the formation of asymmetric structures in PADs.

II. SIMULATION METHOD

The QTMC model [28] is used to study the PADs in two-color laser fields with parallel polarizations. The two-color fields are given by

$$\mathbf{E}(t) = E_0 f(t) [\cos(\omega t) + \alpha \cos(2\omega t + \varphi)] \mathbf{z}, \quad (1)$$

where ω and E_0 are the frequency and amplitude of the 800-nm fundamental laser field, $f(t)$ is the pulse envelope, φ is the relative phase, α is the ratio of field strength of the two frequency components ($\alpha = 0.3$), and \mathbf{z} represents the laser polarization direction. Atomic units are used throughout unless specified otherwise. We take hydrogen as a model atom for discussion. In the simulation, the two-color laser field has an eight-cycle trapezoidal envelope with a two-cycle turn on and turn off for the 800-nm field. The typical laser field for $\varphi = 0$ is shown in Fig. 1. In this model, the time-dependent tunneling ionization rate and the initial momentum distribution transverse to the instantaneous laser field direction are given by the Ammosov-Delone-Krainov theory [30,31]. The initial longitudinal momentum is assumed to be zero. Therefore, each trajectory is weighted by

$$\begin{aligned} W(t_0, p_{\perp}^i) &= W_0(t_0) W_1(p_{\perp}^i), \\ W_0(t_0) &\propto [(2I_p)^2 / |E(t_0)|]^2 / \sqrt{2I_p - 1} \\ &\quad \times \exp[-2(2I_p)^{3/2} / |3E(t_0)|], \\ W_1(p_{\perp}^i) &\propto [\sqrt{2I_p} / |E(t_0)|] \exp[-\sqrt{2I_p} (p_{\perp}^i)^2 / |E(t_0)|], \end{aligned} \quad (2)$$

where t_0 is the ionization time and p_{\perp}^i is the initial transverse momentum. The tunnel exit is given by Landau's effective potential theory [32]. After sampling the electrons, their classical motion in the combined laser and the Coulomb field are governed by the Newtonian equation,

$$\ddot{\mathbf{r}} = -\frac{\mathbf{r}(t)}{r^3} - \mathbf{E}(t). \quad (3)$$

The phase factor of each trajectory is given by e^{iS} , where S is the classical action along the trajectory,

$$S = \int_{t_0}^{+\infty} \left[\frac{\mathbf{v}(t)^2}{2} - \frac{1}{|\mathbf{r}(t)|} + I_p \right] dt. \quad (4)$$

The electron asymptotic momenta on the virtual detector are transformed from the electron momentum $\mathbf{q} = \mathbf{q}(t_0, p_{\perp}^i, \tau_L)$ and its position $\mathbf{r} = \mathbf{r}(t_0, p_{\perp}^i, \tau_L)$ at the end of the laser pulse (τ_L is the pulse duration) [33,34],

$$\mathbf{P} = P \frac{P(\mathbf{L} \times \mathbf{a}) - \mathbf{a}}{1 + P^2 L^2}. \quad (5)$$

Here $\mathbf{L} = \mathbf{r} \times \mathbf{q}$ is the angular momentum, and $\mathbf{a} = \mathbf{q} \times \mathbf{L} - \mathbf{r}/r$ is the Runge-Lenz vector. The magnitude of asymptotic momentum P is determined by energy conservation $q^2/2 - 1/r = P^2/2$.

Finally, we collect the asymptotic momenta of all trajectories one by one into an interval of $[-2.5, 2.5] \times [-2.5, 2.5]$ ($p_z \times p_x$) with 1001×1001 bins. Here we restrict the electrons to motion on the $z-x$ polarization plane with $y = 0$ due to the cylindrical symmetry about the z axis. The trajectories will interfere with each other when their asymptotic momenta are in the same bin. The probability of each bin is determined by adding all trajectories in that bin,

$$|A|^2 = \left| \sum_k \sqrt{W(t_0, p_{\perp}^k)} \exp(iS) \right|^2, \quad (6)$$

where k is the k th electron trajectory in that bin. The final momentum distribution is obtained after the probability of all the bins is calculated.

To validate the simulated results by the QTMC model, we have also numerically solved the three-dimensional TDSE in the length gauge of the dipole approximation,

$$i \frac{\partial |\psi(t)\rangle}{\partial t} = \left\{ -\frac{\Delta}{2} - \frac{1}{r} + zE(t) \right\} |\psi(t)\rangle. \quad (7)$$

Starting from the initial $1s$ ground-state orbitals of the hydrogen atom, the wave function is propagated in time using the splitting-operator method [35]. Due to the cylindrical symmetry of the atom in a linearly polarized laser field, the magnetic quantum number is conserved during the propagation. The ionization probability of the asymptotic momentum is obtained as a projection of the final wave function onto the incoming Coulomb waves of the field-free Hamiltonian [36].

III. RESULTS AND DISCUSSIONS

The PADs in linearly polarized monochromatic and dichromatic fields by the QTMC model and the TDSE calculation are shown in Figs. 2 and 3, respectively. One can find that the QTMC simulations agree well with the results of the TDSE. The QTMC result reveals similar interference features with the TDSE result. In monochromatic laser fields [Figs. 2(a) and 3(a)], the PADs are symmetric with respect to the axis $p_z = 0$. After adding a weak doubled-frequency field, the PADs show an asymmetric distribution. Interestingly, the yields of the high-energy photoelectrons and the low-energy photoelectrons exhibit different modulations with respect to the relative phase of the two frequency components, e.g., when

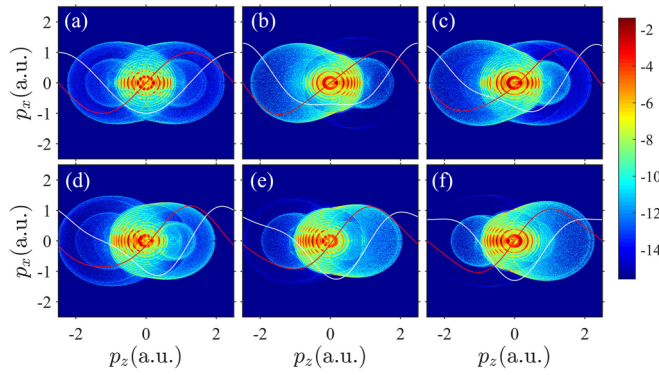


FIG. 2. (Color online) The simulated PADs of H atoms by the QTMC calculations (a) in a linearly polarized laser field and (b)–(f) in a two-color laser field with the Coulomb potential. The relative phases are $\varphi = 0, \pi/4, \pi/2, 3\pi/4,$ and π for (b)–(f), respectively. The white and red (gray) lines show one cycle of the laser field and vector potential in arbitrary units. The laser intensity is $1 \times 10^{14} \text{ W/cm}^2$, $\alpha = 0.3$, $\omega = 0.057$, and $I_p = 0.5$.

$\varphi = 0$, the high-energy photoelectrons are mostly distributed in the region $p_z < 0$ whereas the low-energy photoelectrons are mostly distributed in the region $p_z > 0$. The modulations of both the high-energy photoelectrons and the low-energy photoelectrons with respect to the relative phase by the QTMC calculations are in good agreement with the TDSE results. Next, we will discuss the phase dependence of these two parts of photoelectrons.

In Fig. 4, we show the high-energy cutoff for the negative and positive momenta along the laser polarization direction with respect to the relative phase in the two-color laser field by the QTMC model. We observe the high-energy cutoff can be controlled through the change in the relative phase φ . When $p_z < 0$, the cutoff momentum first increases with the increase of the relative phase, reaches the largest value at about $\varphi = 0.7\pi$, and then decreases. When $p_z > 0$, the change is opposite—the cutoff momentum decreases at first, reaches the smallest value at about $\varphi = 0.6\pi$, and then increases.

We explain the change in cutoff with the help of the classical rescattering model [4]. The electrons which are ionized at t_0

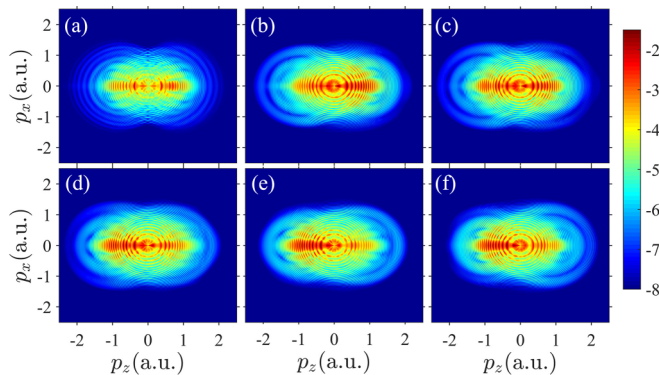


FIG. 3. (Color online) The same as Fig. 2 but by the TDSE calculation.

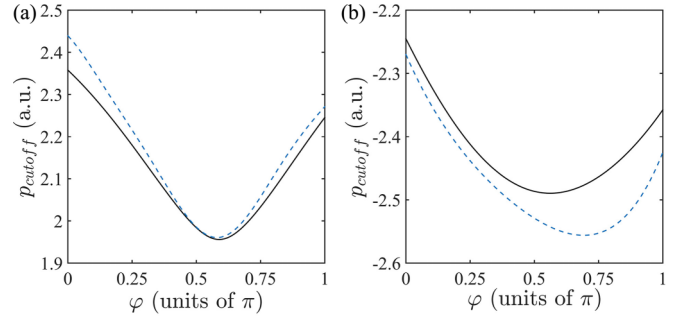


FIG. 4. (Color online) (a) and (b) show the cutoff of the positive momentum and the negative momentum along the laser polarization with respect to the relative phase φ calculated by the classical scattering model (solid black line) and the QTMC model (dashed blue line), respectively.

and return to the nucleus at t_c satisfy the equation,

$$-A(t_0)(t_c - t_0) + \int_{t_0}^{t_c} A(\tau) d\tau = -z_0, \quad (8)$$

where $z_0 = I_p/E_0$ is the position of the tunnel exit. If we consider the backscattering case (the scattering angle is 180°), the final momentum is given by

$$p_z = A(t_0) - 2A(t_c). \quad (9)$$

To get the cutoff momentum, we are supposed to find the maximal and minimal values of Eq. (9) under the condition of Eq. (8).

The change in the cutoff momentum with the relative phase φ based on the classical rescattering model is also shown in Fig. 4 by the solid black curves. We can see that the changes in cutoff energy based on the QTMC and the classical rescattering models are similar except that the cutoff energy in the QTMC model is a little larger than that in the classical scattering model. This difference may originate from the assumption of zero initial transverse momentum in the classical rescattering model [37]. Since we have used the Coulomb potential in the QTMC model whereas a hard-sphere potential is used in the classical scattering model (here the radius of the hard sphere goes to zero), the similarity between these two simulation results manifests that the change in the cutoff energy is mainly a result of the scattering process itself. The long-range Coulomb tail has a minor effect on the position of the cutoff in the energy spectrum.

Now let us turn to the phase-dependent asymmetric structures of the low-energy photoelectron. We show the electron distributions at low energy with considering the Coulomb potential by TDSE calculations and QTMC model in Figs. 5(a) and 5(b), respectively. We can see the low-energy electron distributions of the QTMC results show the same asymmetrical structures as those of the TDSE calculation. The PADs without considering the Coulomb potential by the QTMC model are shown in Fig. 5(c). With neglecting the Coulomb potential, the PADs are asymmetric for $\varphi = \pi/4, \pi/2,$ and $3\pi/4$, and they are symmetric with respect to the polarization axis when $\varphi = 0$ and $\varphi = \pi$. This symmetric distribution can be understood within a simple picture: The electron momentum at the end of laser pulse is determined by the vector potential at the

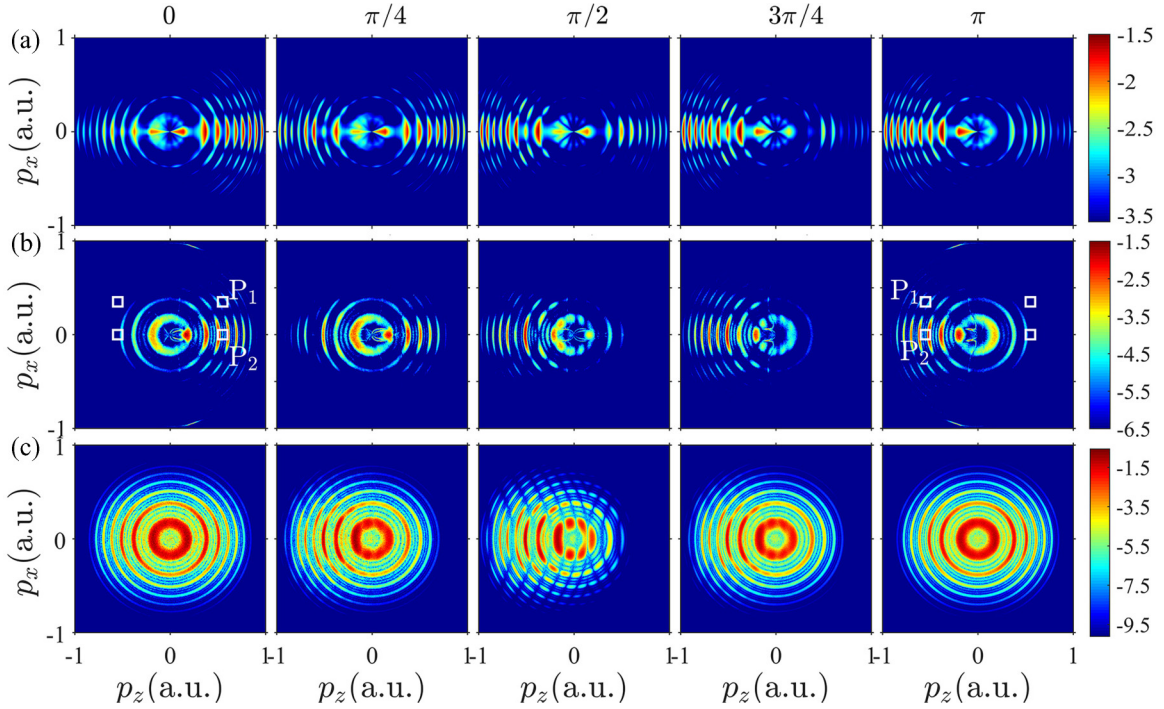


FIG. 5. (Color online) The simulated angular distributions of the low-energy electrons with including the Coulomb potential at $\varphi = 0, \pi/4, \pi/2, 3\pi/4$, and π by (a) TDSE calculations and (b) the QTMC model. (c) shows the simulated PADs without considering the Coulomb potential and the scattering effect by the QTMC model. All parameters used are the same as in Fig. 2. Note the scale is different from Fig. 2.

ionization moment [$p_z = -A(t_0), p_x = p_{\perp}^i$]. For two groups of electrons with a specific final momentum that are symmetric about $p_z = 0$ axis [$p_{1x} = p_{2x}, p_{1z} = -p_{2z}$], their initial classical coordinates satisfy $A(t_1) = -A(t_2), p_{1\perp}^i = p_{2\perp}^i$, corresponding to $E(t_1) = E(t_2)$ when $\varphi = 0$ and $\varphi = \pi$ (see Fig. 2). According to Eq. (2), these two groups of electrons will have the same ionization probability, which leads to symmetric distributions of electron yields with respect to the axis $p_z = 0$. When the Coulomb potential is considered, the low-energy electron momentum distributions become asymmetric for all the phases, including $\varphi = 0$ and $\varphi = \pi$ [e.g., see P_1 and P_2 in Fig. 5(b)]. This demonstrates the importance of the Coulomb potential in the formation of asymmetrical low-energy electron distributions.

To study the effect of the Coulomb potential on the asymmetric low-energy electron distributions, we sample electrons on the right side ($p_z > 0$) and the left side ($p_z < 0$) with respect to the $p_z = 0$ axis [see the white squares in Fig. 5(b)] and trace the electron trajectories back to the initial classical coordinates, i.e., the ionization time and the initial transverse momentum. For simplicity, we will focus on the structures P_1 and P_2 shown in Fig. 5 when $\varphi = 0$ and $\varphi = \pi$. As we will see below, the Coulomb potential mainly affects the formation of the asymmetrical structures in PADs in two ways: (i) another group of rescattered electrons will contribute to the formation of P_1 and P_2 in the presence of the Coulomb potential; (ii) the initial coordinates (ionization time and initial momentum) of the electron trajectories finally contributing to the P_1 and P_2 structures will be corrected by the Coulomb potential.

For the asymmetry of the P_1 structure, it is mainly caused by the first way. Similar to Ref. [28], we find that the P_1 structure is the result of interference among three

different groups of tunneled electrons: (i) forward scattered electrons with large positive initial transverse momentum (R_1), (ii) forward scattered electrons with small negative initial transverse momentum (R_2), and (iii) direct electrons (D) [see Figs. 6(a) and 6(b)]. If the Coulomb effect is not considered, only the groups of R_1 and D will contribute to the formation of structure P_1 [see Figs. 6(c) and 6(d)], which results in symmetric photoelectron distributions when $\varphi = 0$ and $\varphi = \pi$ [see Fig. 5(c)]. In the presence of the Coulomb potential, another group of rescattered electrons (R_2) will significantly contribute to P_1 . Moreover, from Fig. 6(a), we can clearly see that the R_{2R} electrons dominate when $\varphi = 0$ since these electrons ionized at the largest instantaneous electric field and have the smallest initial transverse momenta among all groups of electrons that contribute to the P_1 structure. The ionization amplitudes of all groups of electrons have been shown in Fig. 6. When $\varphi = \pi$, R_{2L} electrons become the dominant electrons [Fig. 6(b)]. Accordingly, the P_1 structure can only be visible on the right (left) side when $\varphi = 0(\varphi = \pi)$.

As for the asymmetry of the P_2 structure, Coulomb correction to the initial conditions of the electron trajectories is the major reason. From Figs. 6(e) and 6(f), we can see that the P_2 structure is a result of interference between two groups of tunneled electrons: (i) forward scattered electrons with positive or negative transverse momentum that have the same magnitude (R) and (ii) direct electrons (D). For electrons with a given final momentum, the ionization time in the presence of the Coulomb potential is earlier than that without considering the Coulomb potential [see the black dashed lines in Fig. (6)] [38]. When $\varphi = 0$, we can first take no account of D_R and R_L electrons because the instantaneous electric field is much weaker than that of the R_R and D_L electrons. As for the R_R

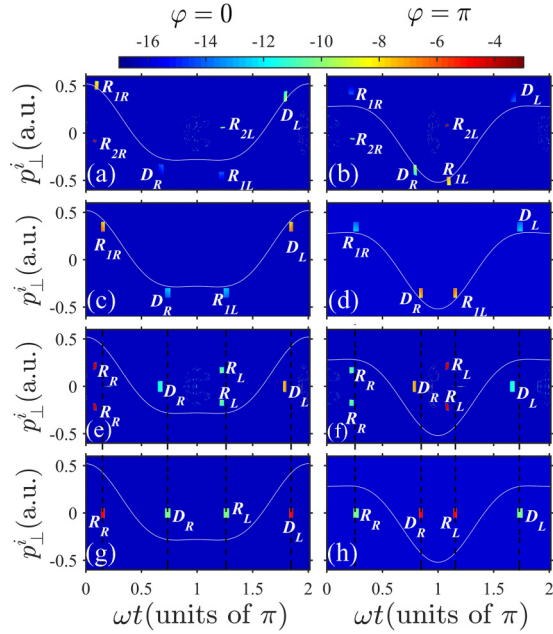


FIG. 6. (Color online) (a)–(h) show the ionization probability of the initial transverse momentum with respect to the tunneling phase of electrons for P_1 [(a)–(d)] and P_2 [(e)–(h)] structures in Fig. 5(b). The first column is $\varphi = 0$, and the second column is $\varphi = \pi$. (a), (b), (e), and (f) have considered the Coulomb potential. (c), (d), (g), and (h) have neglected the Coulomb potential. D and $R_{1(2)}$ stand for the direct electrons and rescattered electrons, respectively. R and L in the subscripts stand for electrons finally distributing on the right side ($p_z > 0$) and the left side ($p_z < 0$), respectively. The vertical black dashed lines show that the ionization time is earlier with considering the Coulomb potential than that without considering the Coulomb potential. A logarithmic scale has been used in the color bar to describe the ionization amplitude.

and D_L electrons, which should have the same ionization amplitude without considering the Coulomb potential [see Fig. 6(g)], we can see in Fig. 6(e) that, due to the Coulomb correction to the ionization time, the R_R electrons are ionized at a stronger electric field and have a larger ionization amplitude whereas the D_L electrons are ionized at a weaker electric field and have a smaller ionization amplitude. Accordingly, when $\varphi = 0$, the R_R electrons dominate, and the P_2 structure is visible on the right side. In a similar way, when $\varphi = \pi$, the R_L electrons dominate, and thus the P_2 structure is visible on the left side.

In the above analysis we have studied the physical origins of the asymmetrical structures P_1 and P_2 when $\varphi = 0$ and $\varphi = \pi$. With the help of the QTMC model, we can also trace back to the initial coordinates of the photoelectrons

at any other relative phase and reveal the origin of the corresponding PADs. Due to the backward scattering, the high-energy photoelectrons exhibit different asymmetries compared to the low-energy photoelectrons as seen in Fig. 2. Moreover, because the electrons tunneled at different ionization times t_0 within half a laser cycle ($T_0/2 = 1.33$ fs) will be streaked to different final momentum, the subcycle interference patterns in the final momentum distribution have recorded attosecond time-resolved electron dynamics. By changing the relative phase of the two-color components, we can control the electron emission time and electron interference patterns with attosecond precision as seen in Fig. 6.

Another interesting phenomenon in the low-energy electron distributions is that the spot patterns which form the first ATI ring in a monochromatic field disappear in the two-color field when $\varphi = 0, \pi/4$, and π [see Fig. 2]. This is caused by the large difference in ionization amplitudes among different groups of tunneled electrons. We have known from Ref. [28] that the spot patterns come from the interference among three different groups of electron trajectories. When $\varphi = 0, \pi/4$, and π , only one group of electrons dominates, which makes the interference effect largely suppressed, and thus the spot patterns induced by the constructive and destructive interference disappear.

IV. CONCLUSION

To summarize, we have comprehensively investigated the control of high-energy cutoff and the asymmetry of low-energy electron distributions in parallelly polarized two-color laser fields. We get similar changes in the cutoff energy with respect to the relative phase using both the classical rescattering model and the QTMC model. We study the phase dependence of the interference structure, which has encoded phase-sensitive electron dynamics in a two-color field. The modulation of the interference patterns with respect to the relative phase in atoms has been used to extract the phase information of electronic wave packets in momentum space [22]. Because the tunneled electron wave packet has encoded the molecular structural information, one may retrieve this structural information from the phase-dependent photoelectron interference patterns. Therefore, extending the two-color scheme to molecules will provide an alternative approach to probe the structural information of molecules in photoelectron holography.

ACKNOWLEDGMENT

We acknowledge support by the National Program on Key Basic Research Project (Project No. 2013CB922403) and the NSFC (Grants No.11434002 and No.11125416).

- [1] L. V. Keldysh, Sov. Phys. JETP **20**, 1037 (1965).
 [2] Y. Huismans, A. Rouzée, A. Gijsbertsen, J. H. Jungmann, A. S. Smolkowska, P. S. W. M. Logman, F. Lépine, C. Cauchy, S. Zamith, T. Marchenko, J. M. Bakker, G. Berden, B. Redlich, A. F. G. van der Meer, H. G. Muller, W. Vermin, K. J. Schafer,

- M. Spanner, M. Y. Ivanov, O. Smirnova, D. Bauer, S. V. Popruzhenko, and M. J. J. Vrakking, *Science* **331**, 61 (2011).
 [3] Y. Huismans, A. Gijsbertsen, A. S. Smolkowska, J. H. Jungmann, A. Rouzée, P. S. W. M. Logman, F. Lépine, C. Cauchy, S. Zamith, T. Marchenko, J. M. Bakker, G. Berden, B. Redlich,

- A. F. G. van der Meer, M. Y. Ivanov, T.-M. Yan, D. Bauer, O. Smirnova, and M. J. J. Vrakking, *Phys. Rev. Lett.* **109**, 013002 (2012).
- [4] G. G. Paulus, W. Becker, W. Nicklich, and H. Walther, *J. Phys. B: At., Mol. Opt. Phys.* **27**, L703 (1994).
- [5] G. G. Paulus, W. Nicklich, and H. Walther, *Europhys. Lett.* **27**, 267 (1994).
- [6] G. G. Paulus, W. Nicklich, H. Xu, P. Lambropoulos, and H. Walther, *Phys. Rev. Lett.* **72**, 2851 (1994).
- [7] P. Agostini, F. Fabre, G. Mainfray, G. Petite, and N. K. Rahman, *Phys. Rev. Lett.* **42**, 1127 (1979).
- [8] D. G. Arbó, K. L. Ishikawa, K. Schiessl, E. Persson, and J. Burgdörfer, *Phys. Rev. A* **81**, 021403(R) (2010).
- [9] D. D. Hickstein, P. Ranitovic, S. Witte, X.-M. Tong, Y. Huismans, P. Arpin, X. Zhou, K. E. Keister, C. W. Hogle, B. Zhang, C. Ding, P. Johnsson, N. Toshima, M. J. J. Vrakking, M. M. Murnane, and H. C. Kapteyn, *Phys. Rev. Lett.* **109**, 073004 (2012).
- [10] X. B. Bian, Y. Huismans, O. Smirnova, K.-J. Yuan, M. J. J. Vrakking, and A. D. Bandrauk, *Phys. Rev. A* **84**, 043420 (2011).
- [11] X. B. Bian and A. D. Bandrauk, *Phys. Rev. Lett.* **108**, 263003 (2012); M. Li *et al.*, *Sci. Rep.* **5**, 8519 (2015).
- [12] O. Smirnova, Y. Mairesse, S. Patchkovskii, N. Dudovich, D. Villeneuve, P. Corkum, and M. Y. Ivanov, *Nature (London)* **460**, 972 (2009).
- [13] G. G. Paulus, F. Lindner, H. Walther, A. Baltuška, E. Goulielmakis, M. Lezius, and F. Krausz, *Phys. Rev. Lett.* **91**, 253004 (2003).
- [14] F. Krausz and M. Ivanov, *Rev. Mod. Phys.* **81**, 163 (2009).
- [15] D. B. Milošević, G. G. Paulus, D. Bauer, and W. Becker, *J. Phys. B: At., Mol. Opt. Phys.* **39**, R203 (2006).
- [16] R. A. Blank and M. Shapiro, *Phys. Rev. A* **52**, 4278 (1995).
- [17] S. Watanabe, K. Kondo, Y. Nabekawa, A. Sagisaka, and Y. Kobayashi, *Phys. Rev. Lett.* **73**, 2692 (1994).
- [18] L. J. Zipp, A. Natan, and P. H. Bucksbaum, in *CLEO: 2014*, OSA Technical Digest (online) (Optical Society of America, 2014), paper FTu1D.3.
- [19] L. J. Zipp, A. Natan, and P. H. Bucksbaum, *Optica* **1**, 361 (2014).
- [20] I. Babushkin, W. Kuehn, C. Köhler, S. Skupin, L. Bergé, K. Reimann, M. Woerner, J. Herrmann, and T. Elsaesser, *Phys. Rev. Lett.* **105**, 053903 (2010).
- [21] D. Zhang, Z. Lü, C. Meng, X. Du, Z. Zhou, Z. Zhao, and J. Yuan, *Phys. Rev. Lett.* **109**, 243002 (2012).
- [22] X. Xie, S. Roither, D. Kartashov, E. Persson, D. G. Arbó, L. Zhang, S. Gräfe, M. S. Schöffler, J. Burgdörfer, A. Baltuška, and M. Kitzler, *Phys. Rev. Lett.* **108**, 193004 (2012).
- [23] D. G. Arbó, S. Nagele, X.-M. Tong, X. Xie, M. Kitzler, and J. Burgdörfer, *Phys. Rev. A* **89**, 043414 (2014).
- [24] S. Skruszewicz, J. Tiggesbäumker, K.-H. Meiwes-Broer, M. Arbeiter, T. Fennel, and D. Bauer, *Phys. Rev. Lett.* **115**, 043001 (2015).
- [25] M. Richter, M. Kunitski, M. Schöffler, T. Jahnke, L. P. H. Schmidt, M. Li, Y. Liu, and R. Dörner, *Phys. Rev. Lett.* **114**, 143001 (2015).
- [26] M. Li, J.-W. Geng, M.-M. Liu, X. Zheng, L.-Y. Peng, Q. Gong, and Y. Liu, *Phys. Rev. A* **92**, 013416 (2015).
- [27] L. Zhang, X. Xie, S. Roither, Y. Zhou, P. Lu, D. Kartashov, M. Schöffler, D. Shafir, P. B. Corkum, A. Baltuška, A. Staudte, and M. Kitzler, *Phys. Rev. Lett.* **112**, 193002 (2014).
- [28] M. Li, J.-W. Geng, H. Liu, Y. Deng, C. Wu, L.-Y. Peng, Q. Gong, and Y. Liu, *Phys. Rev. Lett.* **112**, 113002 (2014).
- [29] Y. Shao, M. Li, M.-M. Liu, X. Sun, X. Xie, P. Wang, Y. Deng, C. Wu, Q. Gong, and Y. Liu, *Phys. Rev. A* **92**, 013415 (2015).
- [30] M. V. Ammosov, N. B. Delone, and V. P. Krainov, *Sov. Phys. JETP* **64**, 1191 (1986).
- [31] N. B. Delone and V. P. Krainov, *J. Opt. Soc. Am. B* **8**, 1207 (1991).
- [32] L. D. Landau and E. M. Lifschitz, *Quantum Mechanics (Non-Relativistic Theory)* (Oxford University Press, New York, 1958).
- [33] N. I. Shvetsov-Shilovski, S. P. Goreslavski, S. V. Popruzhenko, and W. Becker, *Laser Phys.* **19**, 1550 (2009).
- [34] N. I. Shvetsov-Shilovski, D. Dimitrovski, and L. B. Madsen, *Phys. Rev. A* **85**, 023428 (2012).
- [35] L. Peng, E. Pronin, and A. Starace, *New J. Phys.* **10**, 025030 (2008).
- [36] J.-W. Geng, L. Qin, M. Li, W.-H. Xiong, Y. Liu, Q. Gong, and L.-Y. Peng, *J. Phys. B: At., Mol. Opt. Phys.* **47**, 204027 (2014).
- [37] J. Yuan, M. Li, X. Sun, Q. Gong, and Y. Liu, *J. Phys. B: At., Mol. Opt. Phys.* **47**, 015003 (2014).
- [38] M. Li, Y. Liu, H. Liu, Q. Ning, L. Fu, J. Liu, Y. Deng, C. Wu, L.-Y. Peng, and Q. Gong, *Phys. Rev. Lett.* **111**, 023006 (2013).